

System-level Analysis of Dual-Mode Networked Sensing: ISAC Integration & Coordination Gains

Yasser Nabil, Hesham ElSawy, Senior Member, IEEE, and Hossam S. Hassanein, Fellow, IEEE

Abstract—This paper characterizes integration and coordination gains in dense millimeter-wave ISAC networks through a dual-mode framework that combines monostatic and multistatic sensing. A comprehensive system-level analysis is conducted, accounting for base station (BS) density, power allocation, antenna misalignment, radar cross-section (RCS) fluctuations, clutter, bistatic geometry, channel fading, and self-interference cancellation (SIC) efficiency. Using stochastic geometry, coverage probabilities and ergodic rates for sensing and communication are derived, revealing tradeoffs among BS density, beamwidth, and power allocation. It is shown that the communication performance sustained reliable operation despite the overlaid sensing functionality. In contrast, the results reveal the foundational role of spatial sensing diversity, driven by the dual-mode operation, to compensate for the weak sensing reflections and vulnerability to imperfect SIC along with interference and clutter. To this end, we identify a system transition from monostatic to multistatic-dominant sensing operation as a function of the SIC efficiency. In the latter case, using six multistatic BSs instead of a single bistatic receiver improved sensing coverage probability by over 100%, highlighting the coordination gain. Moreover, comparisons with pure communication networks confirm substantial integration gain. Specifically, dual-mode networked sensing with four cooperative BSs can double throughput, while multistatic sensing alone improves throughput by over 50%.

Index Terms—Integrated sensing and communication (ISAC), networked sensing, multistatic, millimeter wave, coverage and ergodic rate analysis, stochastic geometry.

I. INTRODUCTION

The sixth-generation (6G) envisions a unified framework for wireless connectivity and precise sensing, using a single waveform for both sensing and communication (S&C) [1]–[6]. This approach, known as Integrated Sensing and Communications (ISAC) [1], [2], leverages shared channel properties, signal processing, and hardware, enabling base stations (BSs) and mobile users (MUs) to function as sensors. ISAC transforms traditional communication infrastructures into large-scale radio sensing systems, enabling reliable communication and supporting applications such as vehicular networks, environmental monitoring, indoor services, industrial automation, and drone-based surveillance [1]–[6]. It also facilitates emerging higher-level applications such as the metaverse, remote surgeries, autonomous driving, and digital twins [1]–[6]. To this end, ISAC offers two fundamental advantages: integration gain and coordination gain [1], [4]. Integration gain stems from the efficient use of shared wireless resources, reducing hardware redundancy and enhancing spectral efficiency. Coordination gain, in turn, arises from the synergy between S&C. Specifically, sensing-assisted communication, where sensing can improve tasks such as reducing beam training overhead [7], and

communication-assisted sensing (or networked sensing), which leverages cellular connectivity for large-scale coordinated sensing with unparalleled capabilities [1]–[3].

Millimeter-wave (mmWave) frequencies are well-suited for ISAC, offering wide bandwidth and narrow beamwidth that enhance communication capacity, radar range, and angular resolutions [1], [3], enabling more accurate object localization [1], [2]. Monostatic ISAC, with co-located transmitter (Tx) and receiver (Rx), allows compact integration and lower computational overhead but may suffer from strong self-interference (SI) as it relies on full-duplex (FD) operation entailing imperfect self-interference cancellation (SIC) [5]. In the absence of FD, multistatic ISAC systems can utilize cellular infrastructure, where signals are transmitted by one Tx BS and received by other Rx BSs. These systems leverage spatial diversity and wide angular observations that can enhance sensing accuracy and reliability, even in the presence of environmental blockages [1]–[3]. However, the reliability of multistatic sensing without FD remains uncertain. Furthermore, the potential impact of networked sensing on the communication function in large cellular systems needs further investigation.

Recent studies have investigated networked sensing in ISAC systems [8]–[13]. For instance, [8] optimizes joint beamforming to enhance sensing signal-to-noise ratio (SNR) while maintaining communication signal-to-interference-plus-noise ratio (SINR) in cellular multistatic ISAC systems, while [9] introduces a coordinated beamforming framework accounting for synchronization errors. In [10], beamfocusing codewords are employed to address near-field and far-field conditions in urban multistatic mmWave ISAC systems. The authors in [11] leverage a cell-free massive MIMO network to maximize sensing performance via power allocation under communication constraints, and [12] proposes a precoder design framework optimizing sensing and communication under coordinated beamforming and multipoint transmission. Additionally, [13] presents a symbol-level cooperative sensing framework enhancing localization and velocity estimation by centralized fusion of multiple monostatic returns. Despite these advancements, these studies focus on multistatic or monostatic sensing from multiple BSs, without exploring dual operation. Furthermore, most overlook interference and clutter analysis, except [11] and [12], which consider interference from a few BSs rather than a large-scale network.

Achieving integration gains in ISAC systems involves overlapping signals in time and frequency, introducing severe interference and clutter effects [1], [2], [5], which intensify in dense deployments, necessitating large-scale system-level analysis [14]. Moreover, recent ISAC research has shifted from traditional radar metrics to SINR-based evaluations, emphasizing accurate interference modeling to capture system dynamics [14], [15]. Effective ISAC system design requires realistic modeling that incorporates interference, clutter, radar cross-section (RCS) fluctuations, and spatial topology [1]–[4]. To this end, stochastic geometry provides

Y. Nabil is with the Electrical and Computer Engineering Department, Queen's University, Kingston, Ontario, Canada. E-mail: yasser.nabil@queensu.ca. H. ElSawy and H. S. Hassanein are with the School of Computing, Queen's University, Kingston, Ontario, Canada. E-mails: hesham.elsawy@queensu.ca and hossam@cs.queensu.ca.

powerful tools for analyzing ISAC network dynamics, enabling large-scale system-level planning [14]–[20]. This is essential for applications requiring extensive surveillance coverage and for integrating ISAC with existing cellular networks [1]–[4].

For instance, [14] develops an information-theoretic framework for evaluating coverage probabilities and ergodic rates in mmWave ISAC networks. The authors in [15] propose a cooperative ISAC scheme using interference nulling via coordinated beamforming to balance S&C performance. Moreover, [16] explores power and spectrum allocation under constraints like small-distance sensing resolution and high data rates, while [17] analyzes ISAC performance in urban environments with blockage effects. Additionally, [18] optimizes spectral and energy efficiency in dense networks through power allocation. While these studies offer valuable system-level insights, they focus on monostatic sensing, overlooking the inherently more complex multistatic scenario. The recent work in [19] studies a large sub-6 GHz ISAC network with joint monostatic and bistatic detection, utilizing additional bistatic radars that listen only within the same cell. However, this approach limits spatial diversity and it also neglects clutter effects. Moreover, [20] provides a system-level analysis of a cooperative ISAC network operating at sub-6 GHz, effectively deriving the Cramér-Rao Lower Bound (CRLB) of localization accuracy, however, it does not incorporate sensing interference or clutter effects.

Though promising, research on networked sensing is still evolving, particularly in assessing performance in large-scale deployments and investigating how cellular architectures can improve spectral efficiency and sensing capabilities while maintaining communication functionality [1]–[4]. To address the identified gaps in the literature, this paper investigates the networked sensing problem in large-scale mmWave ISAC networks, with a focus on downlink communication and location estimation. The main contributions of this work are as follows:

- The work identifies ISAC integration and coordination gains in large-scale mmWave ISAC networks through a well-founded mathematical model - a first in the literature.
- A novel dual-mode networked sensing approach is explored, integrating monostatic and multistatic sensing using a unified ISAC signal, demonstrating meaningful gains even without FD capabilities.
- A realistic system-level analysis is conducted, considering interference and clutter from all BSs and environmental scatterers, revealing critical tradeoffs between S&C across key parameters such as power, beamwidth, and BS density.

This paper demonstrates the resilience of the communication function in the presence of sensing, which can accelerate the adoption of ISAC in mmWave cellular networks. Moreover, the findings indicate that FD capabilities are not a prerequisite for achieving tangible ISAC benefits; instead, multistatic sensing alone can provide reasonable gains. Additionally, the results quantify the added value of incorporating more cooperative BSs on sensing performance, enabling service providers to make informed decisions on the optimal number of cooperative BSs to balance ISAC gains against backhaul requirements.

The structure of the paper is as follows: Section II outlines the system model. Section III details the analysis of the dual-mode networked sensing. Section IV focuses on the communication analysis. Section V discusses the numerical results and simulations. Lastly, Section VI provides the conclusion.

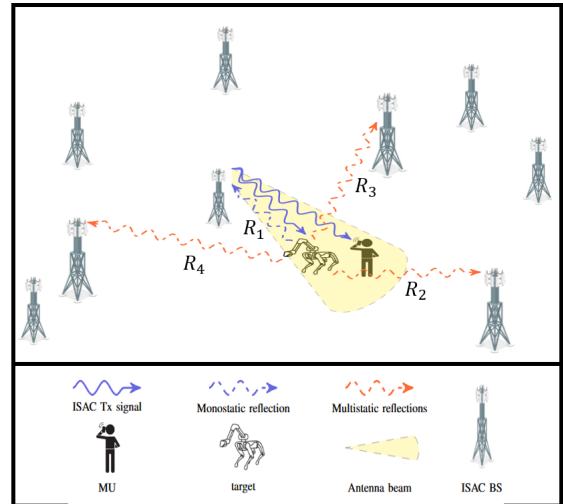


Fig. 1: An illustration of the system model with four cooperative BSs, showing a single beam for clarity. The monostatic distance is R_1 , while each (R_1, R_n) pair forms a bistatic setup, where R_n is the distance between the target and its n^{th} -nearest BS ($n \geq 2$).

II. SYSTEM MODEL

A. ISAC Network and Signal Models

Consider a dense large-scale mmWave network utilizing a unified ISAC waveform. The BSs are spatially distributed as a Poisson Point Process (PPP), Φ_{BS} , with intensity λ_{BS} . Each BS employs multiple spatial beams such that each beam serves a MU while estimating the location of a random target. Operating as a cooperative networked sensing system of N BSs, the serving BS acts as a monostatic radar, receiving echoes from the target, while $(N - 1)$ neighboring BSs receive reflections from the same target in a multistatic configuration.¹ The system is illustrated in Fig. 1.

We adopt a low-complexity unified waveform design of a time slot of duration T_t [21]. The ISAC signal includes a sensing pulse of width T_s , with the remaining time, $T_t - T_s$, allocated for joint communication and sensing (i.e., reception of sensing echoes) as shown in Fig. 2. The sensing pulse duration, T_s , is the reciprocal of the unified signal bandwidth W_b , while T_t is chosen to satisfy the maximum unambiguous range, ensuring that the round-trip time from the farthest target does not exceed T_t . Given a total energy budget E_t per time slot, a bias factor $0 \leq \alpha \leq 1$ allocates α of the energy for the sensing pulse and $(1 - \alpha)$ for communication. Thus, the sensing pulse power is $P_s = \frac{\alpha E_t}{T_s}$, and the communication power is $P_c = \frac{(1-\alpha)E_t}{T_t - T_s}$. This waveform is well-suited for multistatic operations. In monostatic sensing, communication data is transmitted while sensing echoes are received over the same beam, necessitating FD operation with SIC. Given the inherent imperfections of SIC [5], [21], we define ζ as the fraction of power remaining after SIC.

Remark 1. *This design is a unified signal approach, not a time-sharing scheme, enabling simultaneous sensing and communication within the same time and frequency. It preserves communication rates through an extremely short sensing pulse relative to the time slot while ensuring strong sensing performance with a pulse structure featuring favorable correlation properties.*

¹The BSs are interconnected and synchronized via high-speed 5G fronthaul links (typically optical fiber), enabling reliable downlink multistatic sensing and centralized fusion of sensing information [1]–[3].

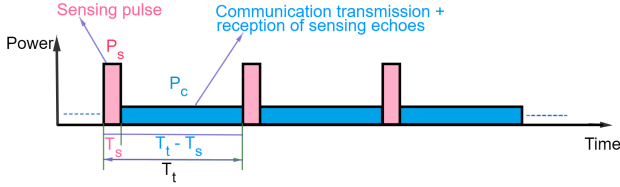


Fig. 2: An illustration for the unified ISAC signal.

B. Beamforming Models

Consider a multi-beam, multi-frequency antenna system where each beam transmits on a distinct frequency but can receive across multiple frequencies. This setup is feasible with modern beamforming techniques and wideband radio frequency (RF) chains, as demonstrated in [22], [23]. To this end, each BS generates M beams covering the 2π space, enabling simultaneous service and sensing of M MUs and M targets per cell.² Each beam operates on a unique frequency block of W_b Hz to transmit the unified ISAC signal, effectively eliminating intra-cell inter-beam interference. Moreover, universal frequency reuse is applied, ensuring full bandwidth utilization across all BSs.

For multistatic operation, signals reflected from targets in neighboring cells randomly arrive at any beam. If a beam receives signals transmitted on any of the $(M - 1)$ frequencies other than its own transmission frequency, these signals are useful for multistatic sensing; otherwise, they are treated as interference. To this end, each BS beam is modeled using the cosine model, which provides precise approximation of the main lobe gains as demonstrated in [24] given by

$$G(\theta) = \begin{cases} G_m \cos^2\left(\frac{d\theta}{2}\right) & |\theta| \leq \frac{\pi}{d} \\ 0 & \text{otherwise} \end{cases}, \quad (1)$$

where G_m represents the maximum gain, d determines the spread of the beam, and θ denotes the beam angle relative to the boresight angle. To ensure complete 2π coverage, the 3-dB beamwidth of each beam is given by $\theta_B = \frac{\pi}{d} = \frac{2\pi}{M}$, where the number of beams is $M = 2d$. Moreover, for simplicity in the analysis, MUs are assumed to use omnidirectional antennas.

C. Channel and Propagation Models

Considering the dense mmWave setup, we adopt the widely used line of sight (LoS) ball model [24]. That is, we assume that the MU and the target maintain a LoS link with the serving BS responsible for monostatic operation. However, the multistatic link between the target and other BSs, as well as co-channel interference signals from other BSs, can be either LoS or non-line of sight (NLoS). According to [25], [26], the probability that a link of distance r is LoS is given by:

$$p_{LOS}(r) = e^{-\gamma r}, \quad (2)$$

where γ is a parameter determined by the density and geometry of the blockage environment.

To ensure tractability and consistency with widely accepted studies [9]–[11], [14], [18], [20], sensing tasks are considered feasible only when a direct LoS link exists between the target and the

²While multiple targets can be sensed per beam if separated by the range resolution, and multiple MUs can be served via user-grouping techniques, this work focuses on a single user and target per beam to reduce analytical complexity. These methods, though enhancing throughput, are left for future work, as the core findings remain valid and extensible to more complex scenarios.

BS. This assumption arises because NLoS channels experience excessive delay and require precise knowledge of the reflection geometry. This challenge is intensified in mmWave channels, where significant attenuation causes multipath components to convey much less reliable information. On the other hand, the communication link and co-channel interference from other BSs are assumed to undergo quasi-static Nakagami- m fading, with fading gains modeled as i.i.d. Gamma random variables (RVs). The shape parameters m_L and m_N correspond to LoS and NLoS conditions, respectively. Furthermore, sensing and communication functions occur within a time slot T_t , during which channel and sensing statistics remain constant but vary across time slots.

Remark 2. *The system's cooperative design introduces spatial diversity, ensuring robust sensing. Even if some cooperative BSs have NLoS links to the target, other BSs with LoS links ensure seamless sensing operation.*

The RCS, which quantifies a target's ability to scatter electromagnetic energy back to the radar, significantly influences the strength of the return signal, directly affecting sensing performance [27], [28]. The monostatic RCS fluctuations of the target, σ_{tm} , is modeled using the Swerling I model [29], which follows an exponential probability density function (PDF), given by:

$$f(\sigma_{tm}) = \frac{1}{\sigma_{av_t}} \exp\left(-\frac{\sigma_{tm}}{\sigma_{av_t}}\right), \quad \sigma_{tm} \geq 0, \quad (3)$$

where σ_{av_t} denotes the average RCS of target. Monostatic setups typically capture stronger reflections, whereas bistatic reflections are weaker and more sensitive to angular variations. Consequently, modeling the bistatic RCS is more challenging, as it depends on the target's capacity to reflect energy from the Tx to the Rx, with the reflection strength heavily influenced by the target's geometry. To account for the impact of bistatic geometry on the target's RCS, we approximate the bistatic RCS, σ_{tb} , following the approach in [30] as

$$\sigma_{tb} \approx \sigma_{tm} \cos\left(\frac{\beta}{2}\right), \quad (4)$$

where β denotes the bistatic angle. This approximation is reasonable, as the high frequency of mmWave ensures that the target's dimensions are significantly larger than the wavelength, making specular reflections dominant while minimizing diffraction and scattering effects [28].

From a sensing perspective, clutter emerges as a new form of interference in ISAC networks, caused by reflections from scatterers other than the targets [1], [2], [5]. As in [31], we model clutter scatterers (cl) as a PPP Φ_{cl} with intensity λ_{Cl} . If the radar resolution cell is defined as the smallest distinguishable unit of space where radar can separate two targets [27], [28], sensing is affected only by clutter from scatterers within the same resolution cell as the target and with comparable RCS. This clutter arrives with nearly the same delay as the target reflection, making it difficult to filter out [32]. Conversely, clutter with significantly different RCS is excluded, as it can be mitigated using standard signal processing techniques [33].

To this end, the monostatic RCS of clutter, σ_{cm} , is modeled using the generalized Weibull distribution, which is widely adopted for its mathematical flexibility in representing diverse

environmental conditions [34] with PDF given by:

$$f(\sigma_{cm}) = \frac{k}{\sigma_{av,cl}} \left(\frac{\sigma_{cm}}{\sigma_{av,cl}} \right)^{k-1} \exp \left(- \left(\frac{\sigma_{cm}}{\sigma_{av,cl}} \right)^k \right), \quad \sigma_{cm} \geq 0, \quad (5)$$

where k denotes the shape parameter, and $\sigma_{av,c}$ represents the average RCS of clutter. In particular, the environment considered here assumes clutter with an RCS comparable to that of the target, which corresponds to an exponential distribution when $k = 1$ [34]. Furthermore, since the clutter RCS is assumed to be comparable to that of the target, its bistatic counterpart, σ_{cb} , can be approximated as in (4) such that $\sigma_{cb} \approx \sigma_{cm} \cos \left(\frac{\beta}{2} \right)$.

III. DUAL-MODE NETWORKED SENSING ANALYSIS

In this section, we carry out the dual-mode networked sensing analysis. We adopt parameter estimation-based formulation for sensing, which is based on mutual information and SINR statistics [14], [15]. The mutual-information-based approach has recently gained widespread adoption in ISAC systems, as it extends the concepts of coverage probability and ergodic rate from communication to sensing, enabling a unified performance evaluation framework for ISAC systems. Specifically, the sensing coverage probability is defined as the probability that the rate of information extracted about a typical target's parameters of interest exceeds some threshold [14]. Meanwhile, the sensing ergodic rate represents the spatial average of this information extraction rate [14], which establishes a theoretical lower bound on estimation error [35]. Mathematically, the sensing coverage probability is expressed as $\mathbb{P}(\text{SINR} > \phi_s)$, where ϕ_s is a predefined threshold [14]. Here, SINR is the ratio of the received sensing signal power to the combined interference, clutter, and noise, where a higher SINR enhances the accuracy of target parameter estimation [36]. Moreover, as derived in [14], [15], the sensing information rate is expressed as:

$$\mathcal{R}_s = \mathbb{E}[\log(1 + \text{SINR})]. \quad (6)$$

A. Types of Interference and Distance Distributions

The different types of interference for sensing, covering both monostatic and bistatic scenarios, are depicted in Fig. 3 and are summarized below:

- 1) **Direct or co-channel interference from other BSs:** represented by red signals in Fig. 3, these signals do not experience the double path-loss affecting the intended sensing signal. They are analyzed under both LoS and NLoS conditions.
- 2) **Intra-clutter interference:** depicted as dashed green signals in Fig. 3, this arises when the intended signal reflects off scatterers within the target's resolution cell. It is analyzed due to its comparable RCS to the target and a similar delay profile, making it difficult to filter out.
- 3) **Inter-clutter interference:** represented by blue signals in Fig. 3, this interference arises from signals originating from other BSs, reflecting off the target or scatterers within the same resolution cell, and reaching the serving BS. These signals can share similar delay or doppler characteristics with the target's echoes, making them difficult to filter out.

The monostatic sensing of a given target is conducted by its nearest BS. Based on the properties of PPP, the PDF of R_1 is:

$$f(R_1) = 2\pi\lambda_{BS}R_1e^{-\pi\lambda_{BS}R_1^2}, \quad R_1 \geq 0. \quad (7)$$

As in [37], the conditional PDF of the distance R_n to the n^{th} nearest BS, given that the distance to the nearest BS is R_1 , is:

$$f(R_n | R_1) = \frac{2(\lambda_{BS}\pi)^{n-1}}{(n-2)!} (R_n^2 - R_1^2)^{n-2} R_n e^{-\lambda_{BS}\pi(R_n^2 - R_1^2)}, \quad 0 \leq R_1 \leq R_n \quad (8)$$

Finally, owing to the structure of the PPP, the angle β between R_1 and R_n is uniformly distributed, with the PDF given by:

$$f(\beta) = \frac{1}{\pi}, \quad 0 \leq \beta \leq \pi. \quad (9)$$

B. Monostatic Sensing Analysis

A generic frequency resource can be utilized by one beam per BS to transmit a unified ISAC signal. To evaluate the SINR, we consider a reference BS at the origin without loss of generality. Direct interference arises when beams from other BSs align with the reference BS's beam on the same frequency block, and inter-clutter interference arises from BSs if their beams are directed toward the target. Following the common practice in stochastic geometry [38], the next approximation captures their impact.

Approximation 1. *To ensure mathematical tractability, direct interfering BSs are approximated by a PPP Φ_s with intensity $\lambda_{I_s} = \frac{\lambda_{BS}}{M^2}$, where $\frac{1}{M^2}$ is the probability of beam alignment between an interfering BS and the typical BS. Moreover, let $\Phi_{L_{IC}}$ denote another PPP of BSs generating inter-clutter signals. These BSs contribute to inter-clutter signals if their beams are directed toward the target with LoS paths and use the same frequency block under analysis. The intensity of this PPP is $\frac{p_{\text{LoS}}(r)\lambda_{BS}}{M}$, where $\frac{1}{M}$ is the probability of a BS beam being directed toward the target.*

The validity of Approximation 1 will be verified through system-level simulations. To this end, the set of interfering BSs, Φ_s , is further divided into two independent PPPs: LOS BSs, Φ_{L_s} , with intensity $p_{\text{LoS}}(r)\lambda_{I_s}$, and NLOS BSs, Φ_{N_s} , with intensity $(1 - p_{\text{LoS}}(r))\lambda_{I_s}$. To estimate location, we consider the monostatic range resolution cell area, defined as $A_{rm} = \frac{c\theta_B R_1}{2W_b}$ [27], where c is the speed of light. This is the smallest region where the radar cannot distinguish closely spaced targets, perceiving them as a single target. Given the typically narrow resolution cell [27] and that only clutter within the same resolution cell as the target is considered, it is reasonable to approximate the range to both as R_1 for tractability. Using the radar range equation [27], the monostatic SINR at the typical BS for a target at R_1 is given in (10) on the next page. The numerator represents the desired echo power, while the denominator represents, intra-clutter, inter-clutter reflected from the target, inter-clutter reflected from other scatterers, thermal noise, LoS direct interference, NLoS direct interference, and residual SI respectively. For simplicity, a constant gain G_m is assumed within the 3-dB beamwidth, while a gain of zero is assumed outside this range. In (10), η_L is the LoS path-loss exponent, and λ is the signal wavelength. Moreover, K_B is the Boltzmann constant, and T is the system temperature. $I_{L_s} = \sum_{BS_i \in \Phi_{L_s}} P_c h_{L,i} G_m^2 C_L r_i^{-\eta_L}$ and $I_{N_s} = \sum_{BS_i \in \Phi_{N_s}} P_c h_{N,i} G_m^2 C_N r_i^{-\eta_N}$, where $h_{L,i}$ and $h_{N,i}$ are the channel gains of the i^{th} LoS and NLoS interfering BS, C_L and C_N are the path-loss intercepts for LoS and NLoS, r_i is the distance between BS_i and the origin, and η_N is the NLOS path-loss exponent.

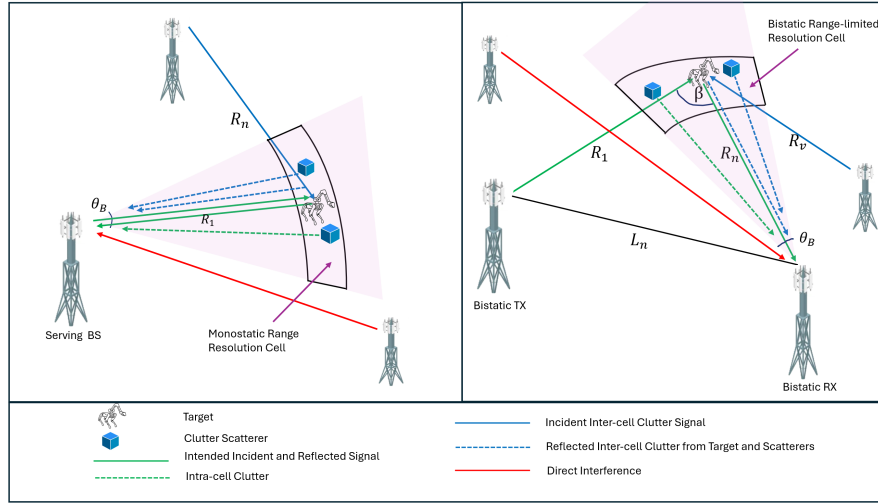


Fig. 3: An illustration depicting interference sources in monostatic operation (left) and bistatic operation (right), where L_n represents the bistatic distance. Each interference type is shown with a single representative signal for clarity.

$$\text{SINR}_M = \frac{\frac{P_s G_m^2 \sigma_{tm} \lambda^2}{(4\pi)^3 R_1^{2\eta_L}}}{\sum_{cl \in \Phi_{cl} \cap A_{rm}} \frac{P_s G_m^2 \sigma_{cm} \lambda^2}{(4\pi)^3 R_1^{2\eta_L}} + \sum_{\substack{\text{BS}_n \in \Phi_{LIC} \\ n \neq 1}} \frac{P_s G_m^2 \sigma_{tb} \lambda^2}{(4\pi)^3 R_1^{\eta_L} R_n^{\eta_L}} + \sum_{\substack{\text{BS}_n \in \Phi_{LIC} \\ n \neq 1}} \sum_{cl \in \Phi_{cl} \cap A_{rm}} \frac{P_s G_m^2 \sigma_{cb} \lambda^2}{(4\pi)^3 R_1^{\eta_L} R_n^{\eta_L}} + K_B T W_b + I_{L_s} + I_{N_s} + P_c \zeta}. \quad (10)$$

Remark 3. Although (10) represents the monostatic SINR, the bistatic RCS appears in the inter-clutter interference terms. This accounts for a bistatic interference setup, where signals from interfering BSs reflect off the target or scatterers in the same resolution cell and return to the serving BS. This interference strength depends on the geometry, captured by the bistatic RCS.

Before evaluating the monostatic sensing coverage probability, we first derive the Laplace transform (LT) of the aggregate interference for different interference types. For direct interference, we define an interference protection region centered at the reference BS (at the origin) with a radius equal to the distance to the nearest neighboring BS, whose PDF is given in (7). The LT of the aggregate direct interference is given in the following lemma.

Lemma 1. The LT of the aggregate direct interference seen by the typical BS located at the origin is given in (11) at the beginning of the next page, where $\mathbf{p}_{LOS}(r)$ is given by (2).

Proof: See Appendix A. ■

The LT of intra-clutter interference, arising from scatterers within the target's resolution cell and with comparable RCS, is presented in the following lemma.

Lemma 2. The LT of monostatic intra-clutter interference is

$$\mathbb{E}_{cl, \sigma_{cm}} \left[\exp \left(- \frac{\phi_s \sum_{cl \in \Phi_{cl} \cap A_{rm}} \sigma_{cm}}{\sigma_{av_t}} \right) \right] = \exp \left(- \lambda_{cl} \frac{c \theta_B R_1}{2W_b} \cdot \frac{\phi_s \sigma_{av_{cl}}}{\sigma_{av_t} + \phi_s \sigma_{av_{cl}}} \right) \quad (12)$$

Proof: See Appendix B. ■

For inter-clutter signals, an interference protection region is established around the target, with a radius corresponding to the distance to the second nearest BS, given that the serving BS is located at R_1 . The PDF of this distance is provided in (8) for

$n = 2$. Accordingly, the LT of inter-clutter interference, including reflections from both the target and other scatterers within the same resolution cell, is presented in the following lemma.

Lemma 3. The LT of monostatic inter-clutter interference is given in (13) on the next page.

Proof: See Appendix C. ■

Building on the previous lemmas, the monostatic sensing coverage probability is presented in the following theorem.

Theorem 1. The monostatic sensing coverage probability for a target at a distance R_1 with SINR threshold ϕ_s is provided in (14) on next page, where $\mathbf{p}_{LOS}(R_1)$ is from (2), the direct interference effect from (11), the intra-clutter effect from (12), and the inter-clutter effect from (13).

Proof: See Appendix D. ■

C. Bistatic Sensing Analysis

Bistatic sensing involves two BSs: the source BS at a distance R_1 from the target and the n^{th} cooperative BS at a distance R_n from the target. The Rx BS can process the bistatic target return through any of its beams, except for the beam that uses the same frequency resource for transmission. In this case, the power of the bistatic reflection is too weak to be processed compared to the monostatic echo. Nevertheless, this reflection contributes to inter-clutter interference in the monostatic scenario. To this end, the SINR for bistatic sensing at the n^{th} -nearest BS from the target is given in (15) on the next page. The numerator represents the desired power received from the target, while the denominator terms correspond to intra-clutter, inter-clutter reflection from the target, inter-clutter reflections from other scatterers, thermal noise, LoS direct interference, and NLoS direct interference. Note that, (15) is free from SI. The bistatic range-limited resolution cell area

$$\begin{aligned} \mathcal{L}_{\text{direct interference}}(s) &= \int_0^\infty \left(\exp \left(-2\pi\lambda_{BS} \frac{1}{M^2} \int_{R_d}^\infty \mathbf{p}_{\text{LOS}}(r) \left(1 - \left(1 + \frac{sP_c G_m^2 C_L r^{-\eta_L}}{m_L} \right)^{-m_L} \right) r dr \right) \right) \\ &\times \exp \left(-2\pi\lambda_{BS} \frac{1}{M^2} \int_{R_d}^\infty (1 - \mathbf{p}_{\text{LOS}}(r)) \left(1 - \left(1 + \frac{sP_c G_m^2 C_N r^{-\eta_N}}{m_N} \right)^{-m_N} \right) r dr \right) \times 2\pi\lambda_{BS} R_d e^{-\pi\lambda_{BS} R_d^2} dR_d \end{aligned} \quad (11)$$

$$\begin{aligned} \mathcal{L}_{\text{inter-clutter}}(s) &= \int_{R_1}^\infty \int_0^\pi \exp \left(-2\pi\lambda_{BS} \frac{1}{M} \int_{R_{IC}}^\infty \mathbf{p}_{\text{LOS}}(r) \left(1 - \frac{1}{1 + s \cos\left(\frac{\beta}{2}\right) r^{-\eta_L} \sigma_{\text{av}_t}} \right) r dr \right) \\ &\times \exp \left(-\lambda_{BS} \cdot \frac{1}{M} \int_{R_{IC}}^\infty \mathbf{p}_{\text{LOS}}(r) \left(1 - \exp \left(-\lambda_{cl} \cdot \frac{c\theta_B R_1}{2W_b} \cdot \frac{s \cos\left(\frac{\beta}{2}\right) r^{-\eta_L} \sigma_{\text{av}_{cl}}}{1 + s \cos\left(\frac{\beta}{2}\right) r^{-\eta_L} \sigma_{\text{av}_{cl}}} \right) \right) 2\pi r dr \right) \\ &\times 2\lambda_{BS} R_{IC} e^{-\lambda_{BS}\pi(R_{IC}^2 - R_1^2)} d\beta dR_{IC} \end{aligned} \quad (13)$$

$$\begin{aligned} \mathcal{P}_M(R_1) &= \underbrace{\mathbb{E}_{cl, \sigma_{cm}} \left[\exp \left(-\frac{\phi_s \sum_{cl \in \Phi_{cl} \cap A_{rb}} \sigma_{cm}}{\sigma_{\text{av}_t}} \right) \right]}_{\text{Intra-clutter effect}} \times \underbrace{\mathcal{L}_{IC1} \left(\frac{\phi_s R_1^{\eta_L}}{\sigma_{\text{av}_t}} \right) \times \mathcal{L}_{IC2} \left(\frac{\phi_s R_1^{\eta_L}}{\sigma_{\text{av}_t}} \right)}_{\text{Inter-clutter effect}} \times \underbrace{\exp \left(-\frac{\phi_s (4\pi)^3 R_1^{2\eta_L} K_B T W_b}{P_s G_m^2 \lambda^2 \sigma_{\text{av}_t}} \right)}_{\text{Noise effect}} \\ &\times \underbrace{\mathcal{L}_{IL_s} \left(\frac{\phi_s (4\pi)^3 R_1^{2\eta_L}}{P_s G_m^2 \lambda^2 \sigma_{\text{av}_t}} \right) \times \mathcal{L}_{IN_s} \left(\frac{\phi_s (4\pi)^3 R_1^{2\eta_L}}{P_s G_m^2 \lambda^2 \sigma_{\text{av}_t}} \right)}_{\text{Direct interference effect}} \times \underbrace{\exp \left(-\frac{\phi_s (4\pi)^3 R_1^{2\eta_L} P_c \zeta}{P_s G_m^2 \lambda^2 \sigma_{\text{av}_t}} \right)}_{\text{Self-interference effect}} \end{aligned} \quad (14)$$

$$\text{SINR}_{B_n} = \frac{\mathbb{1}_{\{c_1\}} \frac{P_s G_m^2 \sigma_{tb} \lambda^2}{(4\pi)^3 R_1^{\eta_L} R_n^{\eta_L}}}{\sum_{cl \in \Phi_{cl} \cap A_{rb}} \frac{P_s G_m^2 \sigma_{cb} \lambda^2}{(4\pi)^3 R_1^{\eta_L} R_n^{\eta_L}} + \sum_{\substack{\text{BS}_v \in \Phi_{LIC} \\ v \neq 1, v \neq n}} \frac{P_s G_m^2 \sigma_{tb} \lambda^2}{(4\pi)^3 R_v^{\eta_L} R_n^{\eta_L}} + \sum_{\substack{\text{BS}_v \in \Phi_{LIC} \\ v \neq 1, v \neq n}} \sum_{cl \in \Phi_{cl} \cap A_{rb}} \frac{P_s G_m^2 \sigma_{cb} \lambda^2}{(4\pi)^3 R_v^{\eta_L} R_n^{\eta_L}} + K_B T W_b + I_{L_s} + I_{N_s}} \quad (15)$$

is A_{rb} , and the indicator function $\mathbb{1}_{\{\cdot\}}$ equals one if $\{\cdot\}$ is true and zero otherwise. The condition c_1 specifies that the target is LoS with the Rx BS, and the bistatic return is received on a different beam than the one using the same frequency, occurring with probability $\frac{M-1}{M}$. Moreover, R_v represents the first link distance for inter-clutter interference between an interfering BS and the target (see Fig. 3).

In the bistatic setup, the range-limited resolution cell is larger and exhibits a more intricate structure than the monostatic one [28]. However, for small bistatic distances L relative to $(R_1 + R_n)$, typical of dense networks, it is approximated as [28], [39]:

$$A_{rb} \approx \frac{cR_n\theta_B}{2W_b \cos^2\left(\frac{\beta}{2}\right)}. \quad (16)$$

For $\beta = 0$, this simplifies to the monostatic case, ensuring consistency between both setups.

Following the same approach used in the monostatic analysis, the LT of various interference sources in bistatic sensing is detailed in the following lemmas.

Lemma 4. *The LT of bistatic intra-clutter interference is:*

$$\begin{aligned} \mathbb{E}_{cl, \sigma_{cm}} \left[\exp \left(-\frac{\phi_s \sum_{cl \in \Phi_{cl} \cap A_{rb}} \sigma_{cm}}{\sigma_{\text{av}_t}} \right) \right] &= \\ \exp \left(-\lambda_{cl} \frac{cR_n\theta_B}{2W_b \cos^2\left(\frac{\beta}{2}\right)} \cdot \frac{\phi_s \sigma_{\text{av}_{cl}}}{\sigma_{\text{av}_t} + \phi_s \sigma_{\text{av}_{cl}}} \right) \end{aligned} \quad (17)$$

Proof: Similar to the proof of Lemma 2, but using the area of bistatic range-limited resolution cell given by (16). ■

Lemma 5. *The LT of bistatic inter-clutter interference is given in (18) at the bottom of the next page.*

Proof: Similar to the proof of Lemma 3, but using the area of bistatic range-limited resolution cell given by (16). ■

Building on the previous lemmas, the bistatic sensing coverage probability is presented in the following theorem.

Theorem 2. *The bistatic sensing coverage probability at the n^{th} nearest BS to the target, where $n \geq 2$, given that the target is at a distance R_1 from the source BS and the SINR threshold is ϕ_s , is expressed in (19) at the bottom of next page, where $\mathbf{p}_{\text{LOS}}(R_n)$ is given by (2), the direct interference effect is given by (11), the intra-clutter effect is given by (17), and the inter-clutter effect is given by (18).*

Proof: See Appendix E. ■

D. The Cooperative Networked Sensing

Building on the monostatic and bistatic sensing coverage probabilities, we analyze the dual-mode cooperative networked sensing, where a target is sensed by its N nearest BSs using monostatic and multistatic operations. While coherent signal combining enhances sensing performance [40], it demands stringent synchronization and precise phase alignment between transmitted

and received signals, making it computationally intensive and costly especially in large-scale multistatic systems [40], [41]. By contrast, the inherent timing differences caused by varying signal travel distances motivate the use of non-coherent processing [41], allowing each BS to handle its received signals independently. To simplify the analysis, we adopt a selection combining strategy, which selects the BS with the highest SINR. This approach ensures reliable performance while reducing computational complexity, backhaul overhead, and signal processing demands. To this end, the networked sensing coverage probability is the probability that the SINR at any of the N cooperative BSs exceeds a threshold ϕ_s , mathematically expressed as:

$$\mathcal{P}_{\text{net}}(R_1) = 1 - \left[(1 - \mathcal{P}_M(R_1)) \prod_{n=2}^N (1 - \mathcal{P}_{B_n}(R_1)) \right]. \quad (20)$$

To evaluate the average cooperative sensing coverage probability, we compute the expectation of (20) with respect to R_1 , whose PDF is given in (7).

Remark 4. (20) is derived as the complement of the probability that none of the cooperative BSs' SINRs exceed the threshold ϕ_s . This assumes independence among the N BSs, justified by the uncertainties in BS locations, LoS conditions, interference, fading gains, RCS fluctuations, and antenna orientations. Nevertheless, the validity of this independence assumption will be further assessed through comprehensive system-level simulations.

E. Sensing information Rate

The sensing rate is quantified using a metric based on the mutual information between sensing returns and the target parameter (i.e., range), capturing the rate at which information about this parameter is acquired. The networked sensing information rate, reflecting the achievable throughput from N cooperative BSs, is derived in the following theorem.

Theorem 3. The average dual-mode networked sensing information rate obtained through cooperation among N BSs is:

$$\mathcal{R}_{s_{\text{avg}}} = M \int_0^\infty \left(\int_0^\infty 1 - \left[(1 - \mathcal{P}_M(R_1, t)) \prod_{n=2}^N (1 - \mathcal{P}_{B_n}(R_1, t)) \right] dt \right) 2\pi\lambda_{BS} R_1 e^{-\pi\lambda_{BS} R_1^2} dR_1 \quad (21)$$

where $\mathcal{P}_M(R_1, t)$ and $\mathcal{P}_{B_n}(R_1, t)$ can be obtained by replacing ϕ_s by $(e^t - 1)$ in Theorem 1 and Theorem 2 respectively.

Proof: Utilizing the integral representation of the expectation of a non-negative RV, the expected value of $\log(1 + \text{SINR}_{\text{net}}(R_1))$ can be expressed as $\int_0^\infty \mathbb{P}(\text{SINR}_{\text{net}}(R_1) > (e^t - 1)) dt$. Hence, the theorem is proved by utilizing the networked sensing coverage probability expression in (20), substituting ϕ_s with $(e^t - 1)$ in Theorems 1 and 2, and then taking the expectation over R_1 . The scaling factor M is included because there are M independent beams, where a target is sensed over each beam simultaneously. ■

IV. COMMUNICATION ANALYSIS

This section focuses on analyzing the communication performance of the proposed ISAC system.

A. SINR Formulation

We start by calculating the SINR at a typical MU, which is assumed to be located at the origin and served by the nearest BS. For mathematical tractability, interfering BSs are divided into two independent PPPs: Φ_{L_c} for LOS BSs with intensity $\mathbf{p}_{\text{LOS}}(r) \times \lambda_{BS}$, and Φ_{N_c} for NLOS BSs with intensity $(1 - \mathbf{p}_{\text{LOS}}(r)) \times \lambda_{BS}$. Moreover, an interference protection region is defined with a radius equal to the distance between the MU and its serving BS, as no other BS can be closer to the MU than the serving BS. Hence, the SINR at the typical MU is given as follows:

$$\text{SINR}_C = \frac{P_c h_{L,o} G(\theta_m) C_L R_o^{-\eta_L}}{I_{L_c} + I_{N_c} + K_B T W_b}, \quad (22)$$

$$\begin{aligned} \mathcal{L}_{\text{inter-clutter}}(s) &= \int_{R_1}^\infty \int_0^\pi \exp \left(-2\pi\lambda_{BS} \frac{1}{M} \int_{R_{IC}}^\infty \mathbf{p}_{\text{LOS}}(r) \left(1 - \frac{1}{1 + s \cos\left(\frac{\beta_I}{2}\right) r^{-\eta_L} \sigma_{\text{av}_t}} \right) r dr \right) \\ &\quad \times \exp \left(-\lambda_{BS} \cdot \frac{1}{M} \int_{R_{IC}}^\infty \mathbf{p}_{\text{LOS}}(r) \left(1 - \exp \left(-\lambda_{cl} \cdot \frac{c R_n \theta_B}{2W_b \cos^2\left(\frac{\beta}{2}\right)} \cdot \frac{s \cos\left(\frac{\beta_I}{2}\right) r^{-\eta_L} \sigma_{\text{av}_{cl}}}{1 + s \cos\left(\frac{\beta_I}{2}\right) r^{-\eta_L} \sigma_{\text{av}_{cl}}} \right) \right) 2\pi r dr \right) \\ &\quad \times 2\lambda_{BS} R_{IC} e^{-\lambda_{BS} \pi (R_{IC}^2 - R_1^2)} d\beta_I dR_{IC} \end{aligned} \quad (18)$$

$$\begin{aligned} \mathcal{P}_{B_n}(R_1) &= \int_{R_1}^\infty \int_0^\pi \frac{\mathbf{p}_{\text{LOS}}(R_n) (M-1)}{M} \times \underbrace{\mathbb{E}_{cl, \sigma_{cm}} \left[\exp \left(-\frac{\phi_s \sum_{cl \in \Phi_{cl} \cap A_{rb}} \sigma_{cm}}{\sigma_{\text{av}_t}} \right) \right]}_{\text{Intra-clutter effect}} \\ &\quad \times \underbrace{\mathcal{L}_{I_{IC1_b}} \left(\frac{\phi_s R_1^{\eta_L}}{\sigma_{\text{av}_t} \cos\left(\frac{\beta}{2}\right)} \right) \mathcal{L}_{I_{IC2_b}} \left(\frac{\phi_s R_1^{\eta_L}}{\sigma_{\text{av}_t} \cos\left(\frac{\beta}{2}\right)} \right)}_{\text{Inter-clutter effect}} \times \underbrace{\exp \left(-\frac{\phi_s (4\pi)^3 R_1^{\eta_L} R_n^{\eta_L} K_B T W_b}{P_s G_m^2 \lambda^2 \cos\left(\frac{\beta}{2}\right) \sigma_{\text{av}_t}} \right)}_{\text{Noise effect}} \\ &\quad \times \underbrace{\mathcal{L}_{I_{L_r}} \left(\frac{\phi_s (4\pi)^3 R_1^{\eta_L} R_n^{\eta_L}}{P_s G_m^2 \lambda^2 \cos\left(\frac{\beta}{2}\right) \sigma_{\text{av}_t}} \right) \mathcal{L}_{I_{N_r}} \left(\frac{\phi_s (4\pi)^3 R_1^{\eta_L} R_n^{\eta_L}}{P_s G_m^2 \lambda^2 \cos\left(\frac{\beta}{2}\right) \sigma_{\text{av}_t}} \right)}_{\text{Direct interference effect}} \frac{2(\lambda_{BS} \pi)^{n-1}}{(n-2)!} (R_n^2 - R_1^2)^{n-2} R_n e^{-\lambda_{BS} \pi (R_n^2 - R_1^2)} \cdot \frac{1}{\pi} d\beta dR_n. \end{aligned} \quad (19)$$

where $h_{L,o}$ represents the fading gain for the intended channel, and R_o denotes the distance of the intended link. The LOS and NLOS interference are expressed as $I_{L_c} = \sum_{\text{BS}_i \in \Phi_{L_c}} P_c h_{L,i} G(\theta_i) C_L r_i^{-\eta_L}$ and $I_{N_c} = \sum_{\text{BS}_i \in \Phi_{N_c}} P_c h_{N,i} G(\theta_i) C_N r_i^{-\eta_N}$, respectively. Here, θ_i is the angle between the line connecting the interfering BS_{*i*} and its intended MU, and the line connecting BS_{*i*} to the reference MU located at the origin.

Remark 5. The possible reflections from targets within the ISAC network at the MU are inherently part of the multipath signals received and are already accounted for in the fading channel gains. However, the impact of introducing sensing on communication in the unified ISAC signal approach appears in key system parameters such as power, beamwidth, and BS density, where the requirements for sensing and communication may conflict (i.e., enhancing one can compromise the other).

B. The Impact of Misalignment Error

Reducing the beamwidth of BS beams improves sensing and communication. Narrower beams enhance antenna gain, boosting communication coverage and rate. For sensing, they improve angular resolution, enable sensing of more targets, and reduce clutter and interference by shrinking the resolution cell area. However, excessively narrow beams make the system prone to misalignment errors, drastically reducing coverage and rate. Thus, it is crucial to study misalignment effects in ISAC networks and determine an optimal beamwidth that balances improved sensing with reliable communication performance. In a realistic scenario, a misalignment error angle θ_m exists between the BS and the MU, caused by various sources of uncertainty. This angle can be modeled as a zero-mean truncated Gaussian RV [42], with $\theta_m \sim N_t(0, a^2, -\theta_M, \theta_M)$, where a^2 denotes the variance and θ_M is the maximum error angle, satisfying $|\theta_M| < \pi$. To proceed with the analysis, the PDF of the antenna gain $G(\theta_m)$ must be derived instead of the PDF of θ_m .

Lemma 6. The PDF of the antenna gain with a truncated Gaussian misalignment error $\theta_m \sim N_t(0, a^2, -\theta_M, \theta_M)$ is

$$f(G_c) = \frac{\sqrt{\frac{2}{d^2 a^2}} \exp\left(-\frac{2}{d^2 a^2} \arccos^2\left(\sqrt{\frac{G_c}{G_m}}\right)\right)}{\text{erf}\left(\frac{\theta_M}{\sqrt{2a^2}}\right) \sqrt{\pi G_c (G_m - G_c)}} \quad (23)$$

where

$$G_c \in \left[G_m \cos^2\left(\frac{d\theta_M}{2}\right), G_m \right] \quad \text{for } |\theta_M| < \frac{\pi}{d}$$

$$G_c \in [0, G_m] \quad \text{for } \frac{\pi}{d} \leq |\theta_M| < \pi$$

Proof: The proof follows starting from the definition of the cumulative distribution function (CDF) of the gain, performing a transformation of a RV based on the relationship between θ_m and $G(\theta_m)$ given in (1), substituting the PDF of θ_m (a truncated Gaussian), and then taking the derivative. ■

C. Communication Coverage Probability

We begin by calculating the LT of the interference.

Lemma 7. The LT of the aggregate LOS and NLOS interference seen by the typical MU located at the origin is given by (24) and (25) respectively.

$$\mathcal{L}_{I_{L_c}}(s) = \exp\left(-\lambda_{BS} \int_{-\frac{\pi}{d}}^{\frac{\pi}{d}} \int_{R_o}^{\infty} \mathbf{P}_{LOS}(r) \left(1 - \left(1 + \frac{s P_c G(\theta_i) C_L r^{-\eta_L}}{m_L}\right)^{-m_L}\right) r dr d\theta_i\right) \quad (24)$$

$$\mathcal{L}_{I_{N_c}}(s) = \exp\left(-\lambda_{BS} \int_{-\frac{\pi}{d}}^{\frac{\pi}{d}} \int_{R_o}^{\infty} (1 - \mathbf{P}_{LOS}(r)) \left(1 - \left(1 + \frac{s P_c G(\theta_i) C_N r^{-\eta_N}}{m_N}\right)^{-m_N}\right) r dr d\theta_i\right) \quad (25)$$

where $\mathbf{P}_{LOS}(r)$ is given in (2).

Proof: See Appendix G. ■

Utilizing the results of Lemma 6 and Lemma 7, the coverage probability is derived in the following theorem.

Theorem 4. The average communication coverage probability with a predefined SINR threshold ϕ_c is given as follows:

$$\mathcal{P}_{com} = \int_0^{\infty} 2\pi \lambda_{BS} R_o e^{-\pi \lambda_{BS} R_o^2} \sum_{n=1}^{m_L} (-1)^{n+1} \binom{m_L}{n} \int \exp\left(-\frac{k_L n \phi_c R_o^{\eta_L} K_B T W_b}{P_c G_c C_L}\right) \mathcal{L}_{I_{L_c}}\left(\frac{k_L n \phi_c R_o^{\eta_L}}{P_c G_c C_L}\right) \mathcal{L}_{I_{N_c}}\left(\frac{k_L n \phi_c R_o^{\eta_L}}{P_c G_c C_L}\right) f(G_c) dG_c dR_o. \quad (26)$$

where $k_L = m_L (m_L!)^{-\frac{1}{m_L}}$, while $\mathcal{L}_{I_{L_c}}$ and $\mathcal{L}_{I_{N_c}}$ are defined in (24) and (25), respectively. Additionally, $f(G_c)$ and its integration limits are provided in Lemma 6.

Proof: See Appendix H. ■

D. Communication Rate

Similar to calculating the sensing rate, the average communication rate per cell is calculated in the following theorem.

Theorem 5. The average communication rate is given as follows:

$$\mathcal{R}_{c,avg} = \frac{M(T_t - T_s)}{T_t} \int_0^{\infty} \mathcal{P}_{com}(t) dt \quad (27)$$

where $\mathcal{P}_{com}(t)$ is given by replacing ϕ_c by $(e^t - 1)$ in Theorem 4, where the term $\frac{T_t - T_s}{T_t}$ is to account for the actual communication duration, and the multiplication by M since a BS is serving M users over M beams simultaneously.

Proof: Similar to the proof of Theorem 3. ■

V. NUMERICAL AND SIMULATION RESULTS

In this section, we first validate the derived formulas using Monte Carlo simulations and examine the influence of various parameters on system performance. We then present system-level design insights, highlighting the coordination and integration gains in large-scale ISAC networks. In each simulation round, two PPP realizations are generated for BSs and clutter scatterers, while MUs and targets are randomly placed within the Voronoi cell of the typical BS. The actual distances between the target and the N nearest cooperative BSs are computed, along with the

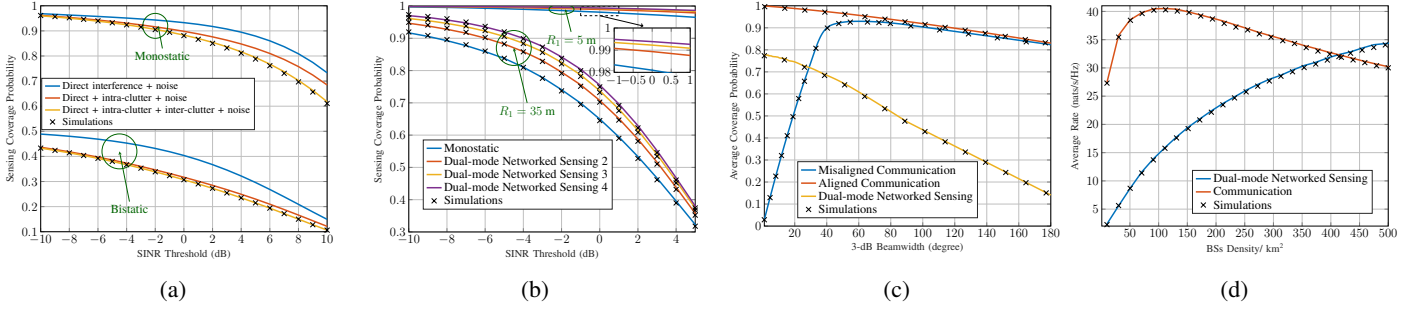


Fig. 4: (a) The effect of different interference types on the monostatic and the bistatic ($n = 2$) operations. (b) The sensing coverage probability for different target locations. (c) The average coverage probability versus beamwidth spread. (d) The average sensing and communication rates versus BS density.

TABLE I: Numerical Parameters

Parameter Description	Symbol	Value
Number of antenna beams	M	12
3-dB beamwidth and spread parameter	θ_B, d	$30^\circ, 6$
Antenna beam maximum gain	G_m	10 dBi
Path loss intercepts	C_L, C_N	-61.4 dB, -72 dB [24]
Path loss exponents	η_L, η_N	2, 4 [24]
Nakagami fading parameters	m_L, m_N	3, 2 [24]
LoS blockage parameter	γ	0.0149 [26]
Bandwidth	W_b	208 MHz [39]
Sensing pulse duration	$T_s = \frac{1}{W_b}$	4.8 ns
Clutter density	λ_{cl}	0.01 m^{-2} [39]
Number of collaborative BSs	N	4
Average RCS of target and clutter	$\sigma_{avt}, \sigma_{av,cl}$	1 m^2 [21], [39]
Transmission powers	P_s, P_c	0.9 W, 0.1 W [21]
Temperature	T	300 K
Time slot duration	T_t	$0.7134 \mu\text{s}$
Fraction of power remaining after SIC	ζ	10^{-12}
Base station density	λ_{BS}	250 BS/km^2
SINR thresholds	ϕ_s, ϕ_c	0 dB
Variance and maximum error angle	α^2, θ_M	1, 0.2π [42]

corresponding bistatic angles. The RCSs of targets and clutter, as well as channel fading gains, are sampled from their respective PDFs. Various types of interference are computed from all BSs based on the actual geometry. The communication SINR is evaluated at the MU, while the sensing SINRs are computed at the N cooperative BSs, with the highest among them selected as the sensing SINR for this realization. Coverage probabilities and rates are obtained by averaging over 2×10^5 simulation runs. The simulation area is 20 km^2 , and the operating frequency lies within the 28 GHz band. Moreover, T_t is calculated such that the maximum unambiguous range is $3R_{\text{eff}}$ [14], where $R_{\text{eff}} = \sqrt{\frac{1}{\pi \lambda_{BS}}}$ represents the effective radius of the Voronoi cell. Unless stated otherwise, all numerical values are taken from Table I.

Fig. 4a depicts the effect of different interference types on monostatic sensing (assuming perfect SIC) and bistatic sensing ($n = 2$) for a target positioned 20 m from the serving BS. The close alignment between analytical results and simulations confirms the validity of Theorem 1 and Theorem 2. The figure demonstrates that focusing on direct (co-channel) interference, as in communication systems, while ignoring clutter-related interference results in overly optimistic sensing coverage estimates. While all interference types contribute comparably in monostatic sensing, their impact on bistatic sensing varies. The larger bistatic resolution cell introduces more scatterers, making intra-clutter interference dominant. Meanwhile, inter-clutter interference is

lower than in the monostatic case due to independent LoS/NLoS conditions for both inter-clutter links (i.e., R_n and R_v) in bistatic scenarios, unlike monostatic sensing, where one inter-clutter link (i.e., R_1) is always LoS. Overall, monostatic sensing achieves higher coverage probability under effective SIC due to proximity to the target, better LoS conditions, higher RCS values with concentrated reflections, and smaller resolution cells that reduce intra-clutter interference.

Fig. 4b illustrates the sensing coverage probability for two scenarios: one with a target near the cell center and the other at a farther location, comparing monostatic sensing with networked sensing involving 2, 3, and 4 BSs. The close match between analytical results and simulations validates (20) for networked sensing fusion, confirming the independence assumption's accuracy. The figure shows that dual-mode networked sensing fusion significantly enhances performance by leveraging spatial diversity. This improvement stems from the fact that, while the average coverage probability of individual bistatic links is lower than that of monostatic ones due to inherent randomness in the network. The figure shows that monostatic sensing is sufficient for targets near the cell center. However, as the target becomes closer to the cell edge, the benefits of networked sensing become more evident, providing significant performance enhancement. While involving additional BSs consistently improves coverage probability, the marginal gains diminish as n increases, making further complexity less practical. Hence, cooperation with a few nearest BSs thus strikes an efficient balance between performance and system complexity.

Fig. 4c shows the average coverage probability for sensing and communication versus 3-dB beamwidth, validating Theorem 4. For sensing, narrower beams improve coverage probability by increasing antenna gain, reducing direct interference, minimizing clutter, and enhancing angular resolution. In communication, narrower beams theoretically improve coverage due to higher gain and reduced interference. However, in practice, coverage peaks at an optimal beamwidth and declines sharply beyond it, as narrower beams provide higher gain but are more sensitive to misalignment. Hence, careful beamwidth selection is essential to balance sensing and communication performance in unified ISAC systems.

Fig. 4d illustrates the relationship between average sensing and communication rates and BS density, validating Theorems 3 and 5. The plot reveals an optimal BS density for maximizing communication rates. At low densities, the system is noise-limited, where increased density shortens link distances, improving coverage and

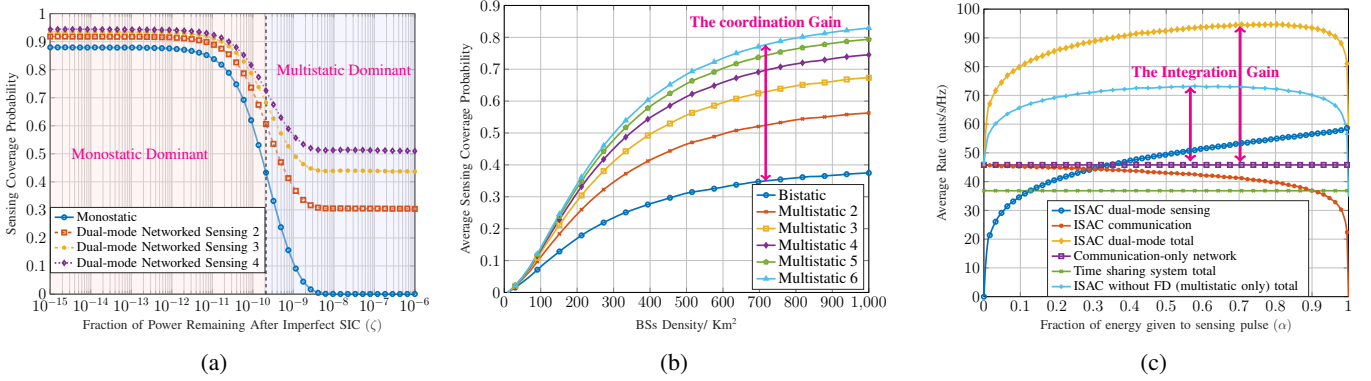


Fig. 5: (a) The effect of imperfect SIC for a target at a range = 20 m. (b) The networked-sensing performance without the monostatic sensing in case FD is not available. (c) The effect of energy allocation between sensing and communication across the ISAC signal.

rates. Beyond this point, the system becomes interference-limited, as higher density transitions more interference links from NLoS to LoS, reducing coverage and rates. In contrast, sensing rates consistently increase with BS density, growing rapidly at first and slowing at higher densities. This behavior is driven by: 1) increased probability of LoS links in multistatic sensing due to shorter distances; 2) the intended sensing signal experiences path loss with an exponent twice that of the direct interference signal, resulting in a greater marginal improvement in intended signal strength as BS density increases; and 3) the reduction in the resolution cell area, which minimizes the impact of clutter. The slower growth at higher densities is due to more interference signals transitioning to LoS, amplifying their impact, but this effect remains outweighed by the three aforementioned factors.

Fig. 5a illustrates the impact of imperfect SIC on sensing coverage probability. Efficient SIC implies negligible residual power, which enables high coverage primarily through monostatic sensing. However, as ζ exceeds a certain threshold, monostatic performance sharply declines to zero, shifting the system to multistatic-dominant sensing. The figure highlights the distinct challenges of FD for sensing compared to communication. While a residual power fraction as small as 10^{-9} is acceptable for FD communication [43], it can severely impair monostatic sensing due to the round-trip path loss unique to sensing. Nonetheless, networked sensing can offer reasonable performance through multistatic contributions, although this demands increased collaboration among more BSs, as detailed in the next figure.

Fig. 5b examines average sensing coverage probability without FD, where monostatic sensing is infeasible, relying instead on multistatic sensing. The figure shows that increasing the number of cooperating BSs improves performance by exploiting spatial diversity, as bistatic RCS is captured from multiple angles. The performance also improves with higher network density, driven by the same factors discussed in Fig. 4d. For instance, when six BSs cooperate in receiving sensing echoes instead of a single BS Rx, the sensing coverage probability increases by **108%** at a BS density of 250 BSs/km² and by **120%** at 500 BSs/km². This improvement is only possible through the cellular infrastructure's networking capabilities and synchronized operation, enabling efficient coordination that standalone sensing systems cannot achieve. This seamless cooperation among BSs highlights the significant coordination gain in ISAC networks.

Fig. 5c analyzes the impact of power allocation on average

information rates, assuming $E_t = 0.2378 \mu\text{Joule}$ (equivalent to 1 W average power per time slot). The results demonstrate the integration gain of the proposed ISAC system, where the total rate significantly exceeds the individual rates of sensing and communication. This gain is maximized by allocating more energy to the sensing pulse, which helps mitigate SI, compensate for round-trip path loss, and reduce direct interference. In dense networks, increasing power has a limited effect on communication performance, as it amplifies both the signal and interference, whereas sensing benefits more directly. Additionally, Fig. 5c compares the proposed system to a time-sharing approach where sensing and communication share equal time sequentially. Although this eliminates SI, the overall performance is very low, as each function is limited to half the time.

To assess the impact of incorporating sensing functionality on communication, the proposed system is contrasted to a communication-only network, where all resources are allocated to communication. The results show that ISAC maintains comparable communication performance while delivering substantial sensing gains. Notably, the total throughput increases by **106%** compared to the communication-only network, highlighting the integration gain of the dual-mode ISAC system. Moreover, Fig. 5c plots the total ISAC rate without FD, relying on multistatic sensing from the nearest six BSs. Remarkably, the system still achieves a meaningful integration gain, with total throughput increasing by **60%** compared to the communication-only network. This demonstrates the proposed ISAC framework's efficiency even without FD technology. Notably, the optimal power to maximize gain in this scenario is lower than in the FD-enabled case, as there is no monostatic operation or residual SI power.

VI. CONCLUSION

The paper studies the integration and coordination gains in large-scale mmWave ISAC networks using a dual-mode sensing framework that combines monostatic and multistatic approaches. System-level analysis revealed that overlooking sensing specific interference sources leads to overestimated performance, with interference impacting monostatic and bistatic sensing differently. Analysis of the unified signal approach shows that BS density, beamwidth, and power allocation involve intricate design trade-offs. Higher BS density improves sensing but communication is optimized at a certain BS density before declining, narrower beams enhance sensing but increase communication misalignment

risks, and allocating more energy to sensing pulse than to the rest of the signal enhances total throughput. Additionally, the results confirm the resilience of communication performance despite the integrated sensing functionality, demonstrating ISAC's feasibility in dense networks.

The findings show that dual-mode cooperative sensing enhances sensing performance by leveraging spatial sensing diversity. Specifically, in scenarios with highly imperfect SIC or without FD, the system transitions to multistatic-dominant operation, maintaining reliable sensing. This performance is further enhanced through network densification and the addition of more cooperative BSs, highlighting the coordination gains in ISAC systems. Comparisons with communication-only and time-sharing systems demonstrate the superior integration gains of the proposed approach. Notably, even in multistatic mode alone, the system achieves a reasonable integration gain, demonstrating that FD is not a strict requirement for ISAC systems. Furthermore, the results highlight the impact of additional cooperative BSs on sensing performance, providing valuable insights for service providers to balance ISAC benefits with backhaul constraints.

APPENDIX A PROOF OF LEMMA 1

Using the definition of LT:

$$\begin{aligned}\mathcal{L}_{I_{L_s}}(s) &= \mathbb{E}_{\Phi_{L_s}, h_{L,i}} [\exp(-sI_{L_s})] \\ &= \mathbb{E}_{\Phi_{L_s}, h_{L,i}} \left[\exp \left(-s \sum_{\text{BS}_i \in \Phi_{L_s}} P_c h_{L,i} G_m^2 C_L r_i^{-\eta_L} \right) \right] \\ &= \mathbb{E}_{\Phi_{L_s}} \left[\prod_{\text{BS}_i \in \Phi_{L_s}} \mathbb{E}_{h_{L,i}} \left[\exp \left(-s P_c h_{L,i} G_m^2 C_L r_i^{-\eta_L} \right) \right] \right].\end{aligned}\quad (28)$$

From the Gamma distribution's moment-generating function:

$$\mathcal{L}_{I_{L_s}}(s) = \mathbb{E}_{\Phi_{L_s}} \left[\prod_{\text{BS}_i \in \Phi_{L_s}} \left(1 + \frac{s P_c G_m^2 C_L r_i^{-\eta_L}}{m_L} \right)^{-m_L} \right]. \quad (29)$$

Consider the closet interfering BS at a distance R_d . Using polar coordinates and the definition of probability generating functional (PGFL) in PPP:

$$\begin{aligned}\mathcal{L}_{I_{L_s}}(s) &= \exp \left(-\frac{2\pi\lambda_{BS}}{M^2} \int_{R_d}^{\infty} \mathbf{p}_{\text{LOS}}(r) \right. \\ &\quad \left. \left(1 - \left(1 + \frac{s P_c G_m^2 C_L r^{-\eta_L}}{m_L} \right)^{-m_L} \right) r dr \right).\end{aligned}\quad (30)$$

For NLOS interference, the previous steps are repeated, replacing $\mathbf{p}_{\text{LOS}}(r)$ by $(1 - \mathbf{p}_{\text{LOS}}(r))$, m_L by m_N , C_L by C_N and η_L by η_N . By combining both formulas and taking the expectations over R_d with PDF defined in (7), the lemma is proved.

APPENDIX B PROOF OF LEMMA 2

Since the intra-clutter contribution involves a random number of scatterers and random RCS within the resolution cell A_{rm} . Therefore, we take the expectation over both the random clutter

scatterers and their RCS, then using the PGFL of PPP:

$$\begin{aligned}&\mathbb{E}_{cl, \sigma_{cm}} \left[\exp \left(-\frac{\phi_s \sum_{cl \in \Phi_{cl} \cap A_{rm}} \sigma_{cm}}{\sigma_{av_t}} \right) \right] \\ &= \mathbb{E}_{cl} \left[\prod_{cl \in \Phi_{cl} \cap A_{rm}} \mathbb{E}_{\sigma_{cm}} \left[\exp \left(-\frac{\phi_s \sigma_{cm}}{\sigma_{av_t}} \right) \right] \right] \\ &= \exp \left(-\lambda_{cl} \int_{A_{rm}} \mathbb{E}_{\sigma_{cm}} \left[1 - \exp \left(-\frac{\phi_s \sigma_{cm}}{\sigma_{av_t}} \right) \right] dA_{rm} \right).\end{aligned}\quad (31)$$

By substituting the monostatic range resolution Cell Area:

$$\begin{aligned}&\mathbb{E}_{cl, \sigma_{cm}} \left[\exp \left(-\frac{\phi_s \sum_{cl \in \Phi_{cl} \cap A_{rm}} \sigma_{cm}}{\sigma_{av_t}} \right) \right] \\ &= \exp \left(-\lambda_{cl} \frac{c\theta_B R_1}{2W_b} \mathbb{E}_{\sigma_{cm}} \left[1 - \exp \left(-\frac{\phi_s \sigma_{cm}}{\sigma_{av_t}} \right) \right] \right).\end{aligned}\quad (32)$$

Since σ_{cm} follows a Weibull distribution given by (5) with shape parameter $k = 1$ which is exponential, then the expectation simplifies to:

$$\mathbb{E}_{\sigma_{cm}} \left[1 - \exp \left(-\frac{\phi_s \sigma_{cm}}{\sigma_{av_t}} \right) \right] = \frac{\phi_s \sigma_{av_{cl}}}{\sigma_{av_t} + \phi_s \sigma_{av_{cl}}}. \quad (33)$$

Thus, by substituting (33) in (32), the lemma is proved.

APPENDIX C PROOF OF LEMMA 3

$$\begin{aligned}\mathcal{L}_{I_{IC1}}(s) &= \mathbb{E}_{\Phi_{L_{IC}}, \sigma_{tm}} [\exp(-sI_{IC1})] \\ &= \mathbb{E}_{\Phi_{L_{IC}}, \sigma_{tm}} \left[\exp \left(-s \sum_{\substack{\text{BS}_n \in \Phi_{L_{IC}} \\ n \neq 1}} \cos \left(\frac{\beta}{2} \right) R_n^{-\eta_L} \sigma_{tm} \right) \right] \\ &= \mathbb{E}_{\Phi_{L_{IC}}} \left[\prod_{\substack{\text{BS}_n \in \Phi_{L_{IC}} \\ n \neq 1}} \mathbb{E}_{\sigma_{tm}} \left[\exp \left(-s \cos \left(\frac{\beta}{2} \right) R_n^{-\eta_L} \sigma_{tm} \right) \right] \right].\end{aligned}\quad (34)$$

Since σ_{tm} is an exponential PDF with mean σ_{av_t} , then:

$$\mathcal{L}_{I_{IC1}}(s) = \mathbb{E}_{\Phi_{L_{IC}}} \left[\prod_{\substack{\text{BS}_n \in \Phi_{L_{IC}} \\ n \neq 1}} \frac{1}{1 + s \cos \left(\frac{\beta}{2} \right) R_n^{-\eta_L} \sigma_{av_t}} \right]. \quad (35)$$

Next, we apply the PGFL of PPP:

$$\begin{aligned}\mathcal{L}_{I_{IC1}}(s) &= \exp \left(-2\pi\lambda_{BS} \times \frac{1}{M} \int_{R_{IC}}^{\infty} \mathbf{p}_{\text{LOS}}(r) \right. \\ &\quad \left. \times \left(1 - \frac{1}{1 + s \cos \left(\frac{\beta}{2} \right) r^{-\eta_L} \sigma_{av_t}} \right) r dr \right).\end{aligned}\quad (36)$$

Similarly, $\mathcal{L}_{I_{IC2}}(s)$ can be expressed as:

$$\begin{aligned}\mathcal{L}_{I_{IC2}}(s) &= \mathbb{E}_{\Phi_{L_{IC}}} \left[\prod_{\substack{\text{BS}_n \in \Phi_{L_{IC}} \\ n \neq 1}} \mathbb{E}_{cl, \sigma_{cm}} \left[\exp \left(-s \cos \left(\frac{\beta}{2} \right) R_n^{-\eta_L} \right. \right. \right. \\ &\quad \left. \left. \left. \sum_{cl \in \Phi_{cl} \cap A_{rm}} \sigma_{cm} \right) \right] \right].\end{aligned}\quad (37)$$

As in the proof of Lemma 2, we apply the PGFL for the clutter scatterers and multiply by the area of the resolution cell:

$$\begin{aligned} & \mathbb{E}_{cl, \sigma_{cm}} \left[\exp \left(-s \cos \left(\frac{\beta}{2} \right) R_n^{-\eta_L} \sum_{cl \in \Phi_{cl} \cap A_{rm}} \sigma_{cm} \right) \right] \\ &= \exp \left(-\lambda_{cl} \cdot \frac{c\theta_B R_1}{2W_b} \cdot \mathbb{E}_{\sigma_{cm}} \left[1 - \exp \left(-s \cos \left(\frac{\beta}{2} \right) R_n^{-\eta_L} \sigma_{cm} \right) \right] \right). \end{aligned} \quad (38)$$

By using the the Weibull distribution when $k = 1$ and compute the expectation over σ_{cm} :

$$\mathbb{E}_{\sigma_{cm}} \left[1 - \exp \left(-s \cos \left(\frac{\beta}{2} \right) R_n^{-\eta_L} \sigma_{cm} \right) \right] = \frac{s \cos \left(\frac{\beta}{2} \right) R_n^{-\eta_L} \sigma_{av,cl}}{1 + s \cos \left(\frac{\beta}{2} \right) R_n^{-\eta_L} \sigma_{av,cl}}. \quad (39)$$

We substitute back into (37), then apply the PGFL for the BSs:

$$\begin{aligned} \mathcal{L}_{LIC2}(s) &= \exp \left(- \int_{R_{IC}}^{\infty} \lambda_{BS} \cdot \frac{1}{M} \cdot \mathbf{p}_{LOS}(r) \right. \\ &\quad \left. \cdot \left(1 - \exp \left(-\lambda_{cl} \cdot \frac{c\theta_B R_1}{2W_b} \cdot \frac{s \cos \left(\frac{\beta}{2} \right) r^{-\eta_L} \sigma_{av,cl}}{1 + s \cos \left(\frac{\beta}{2} \right) r^{-\eta_L} \sigma_{av,cl}} \right) \right) 2\pi r dr \right). \end{aligned} \quad (40)$$

Since R_{IC} and β are two RVs with PDFs given by (8) when $n = 2$ and (9) respectively, then, the lemma is proved by combining both formulas and taking the expectations.

APPENDIX D

PROOF OF THEOREM 1

By simplifying (10) and substituting $\sigma_{tb} = \sigma_{tm} \cos \left(\frac{\beta}{2} \right)$ and $\sigma_{cb} = \sigma_{cm} \cos \left(\frac{\beta}{2} \right)$, and by letting $L_{IC1} = \sum_{\substack{BS_n \in \Phi_{LIC} \\ n \neq 1}} \cos \left(\frac{\beta}{2} \right) R_n^{-\eta_L} \sigma_{tm}$ and

$L_{IC2} = \sum_{\substack{BS_n \in \Phi_{LIC} \\ n \neq 1}} \cos \left(\frac{\beta}{2} \right) R_n^{-\eta_L} \sum_{cl \in \Phi_{cl} \cap A_{rm}} \sigma_{cm}$, then the

monostatic sensing coverage probability can be expressed as:

$$\begin{aligned} \mathcal{P}_M &= \mathbb{P}(\text{SINR}_M > \phi_s) \\ &= \mathbb{P} \left[\sigma_{tm} > \sum_{cl \in \Phi_{cl} \cap A_{rm}} \phi_s \sigma_{cm} + \phi_s R_1^{\eta_L} L_{IC1} + \right. \\ &\quad \left. \phi_s R_1^{\eta_L} L_{IC2} + \frac{\phi_s (4\pi)^3 R_1^{2\eta_L}}{P_s G_m^2 \lambda^2} \left(K_B T W_b + I_{L_r} + I_{N_r} + P_c \zeta \right) \right]. \end{aligned} \quad (41)$$

Using the Swerling I model, with PDF given by (3), Then:

$$\begin{aligned} \mathcal{P}_M &= \exp \left(- \frac{1}{\sigma_{av,t}} \left[\sum_{cl \in \Phi_{cl} \cap A_{rm}} \phi_s \sigma_{cm} + \phi_s R_1^{\eta_L} L_{IC1} \right. \right. \\ &\quad \left. \left. + \phi_s R_1^{\eta_L} L_{IC2} + \frac{\phi_s (4\pi)^3 R_1^{2\eta_L}}{P_s G_m^2 \lambda^2} \left(K_B T W_b + I_{L_r} + I_{N_r} + P_c \zeta \right) \right] \right). \end{aligned} \quad (42)$$

Finally, the expression can be decomposed into terms representing the LT of different interference sources.

APPENDIX E

PROOF OF THEOREM 2

Considering the target in LoS conditions with the Rx, then by simplifying (15) and substituting $\sigma_{tb} = \sigma_{tm} \cos \left(\frac{\beta}{2} \right)$ and $\sigma_{cb} = \sigma_{cm} \cos \left(\frac{\beta}{2} \right)$, and by letting $L_{IC1b} = \sum_{\substack{BS_v \in \Phi_{LIC} \\ v \neq 1, v \neq n}} \cos \left(\frac{\beta}{2} \right) R_v^{-\eta_L} \sigma_{tm}$ and

$L_{IC2b} = \sum_{\substack{BS_v \in \Phi_{LIC} \\ v \neq 1, v \neq n}} \cos \left(\frac{\beta}{2} \right) R_v^{-\eta_L} \sum_{cl \in \Phi_{cl} \cap A_{rb}} \sigma_{cm}$, then the

bistatic sensing coverage probability can be expressed as:

$$\begin{aligned} \mathbb{P}(\text{SINR}_{B_n} > \phi_s) &= \mathbb{P} \left[\sigma_{tm} > \sum_{cl \in \Phi_{cl} \cap A_{rb}} \phi_s \sigma_{cm} + \frac{\phi_s R_1^{\eta_L} L_{IC1b}}{\cos \left(\frac{\beta}{2} \right)} \right. \\ &\quad \left. + \frac{\phi_s R_1^{\eta_L} L_{IC2b}}{\cos \left(\frac{\beta}{2} \right)} + \frac{\phi_s (4\pi)^3 R_1^{\eta_L} R_n^{\eta_L}}{P_s G_m^2 \lambda^2 \cos \left(\frac{\beta}{2} \right)} (K_B T W_b + I_{L_r} + I_{N_r}) \right]. \end{aligned} \quad (43)$$

Again, by adopting the Swerling I model, then:

$$\begin{aligned} \mathbb{P}(\text{SINR}_{B_n} > \phi_s) &= \exp \left(- \frac{1}{\sigma_{av,t}} \left[\sum_{cl \in \Phi_{cl} \cap A_{rb}} \phi_s \sigma_{cm} + \frac{\phi_s R_1^{\eta_L} L_{IC1b}}{\cos \left(\frac{\beta}{2} \right)} \right. \right. \\ &\quad \left. \left. + \frac{\phi_s R_1^{\eta_L} L_{IC2b}}{\cos \left(\frac{\beta}{2} \right)} + \frac{\phi_s (4\pi)^3 R_1^{\eta_L} R_n^{\eta_L}}{P_s G_m^2 \lambda^2 \cos \left(\frac{\beta}{2} \right)} (K_B T W_b + I_{L_r} + I_{N_r}) \right] \right). \end{aligned} \quad (44)$$

By incorporating the probability that the target is LoS with the RX and that the bistatic return occurs on a beam other than the beam using the same frequency, the expression can be decomposed into terms representing the LT of different interference sources. Finally, since R_n and β are RVs with PDFs specified in (8) and (9), the theorem is proved by taking their expectations.

APPENDIX F

PROOF OF LEMMA 7

The proof proceeds similarly to that of Lemma 1, utilizing the definition of LT and the moment-generating function of the Gamma distribution, we can reach:

$$\mathcal{L}_{L_c}(s) = \mathbb{E}_{\Phi_{L_c}} \left[\prod_{BS_i \in \phi_{L_c}} \left(1 + \frac{s P_c G(\theta_i) C_L R_i^{-\eta_L}}{m_L} \right)^{-m_L} \right]. \quad (45)$$

Combining BSs' location with their orientations and from the definition of PGFL in PPP, then:

$$\begin{aligned} \mathcal{L}_{L_c}(s) &= \exp \left(-\lambda_{BS} \int_{-\frac{\pi}{2}}^{\frac{\pi}{2}} \int_{R_o}^{\infty} \mathbf{p}_{LOS}(r) \right. \\ &\quad \left. \left(1 - \left(1 + \frac{s P_c G(\theta_i) C_L R^{-\eta_L}}{m_L} \right)^{-m_L} \right) r dr d\theta_i \right). \end{aligned} \quad (46)$$

For NLOS interference, the same steps are followed using the NLOS parameters.

APPENDIX G

PROOF OF THEOREM 4

$$\begin{aligned} \mathcal{P}_{\text{com}}(R_o) &= \mathbb{P}(\text{SINR}_C > \phi_c) = \mathbb{P} \left(\frac{P_c h_{L,o} G(\theta_m) C_L R_o^{-\eta_L}}{I_{L_c} + I_{N_c} + K_B T W_b} > \phi_c \right) \\ &= \mathbb{P} \left(h_{L,o} > \phi_c R_o^{\eta_L} (P_c G(\theta_m) C_L)^{-1} \times (I_{L_c} + I_{N_c} + K_B T W_b) \right). \end{aligned} \quad (47)$$

Utilizing Alzer's inequality [44]:

$$\begin{aligned} \mathcal{P}_{\text{com}}(R_o) &\approx \sum_{n=1}^{m_L} (-1)^{n+1} \binom{m_L}{n} \\ &\quad \mathbb{E} \left[\exp \left(- \frac{k_L n \phi_c R_o^{\eta_L} (I_{L_c} + I_{N_c} + K_B T W_b)}{P_c G(\theta_m) C_L} \right) \right], \end{aligned} \quad (48)$$

where $k_L = m_L(m_L!)^{-\frac{1}{m_L}}$. Moreover, from the definition of LT, and since Φ_{L_c} and Φ_{N_c} are independent, then:

$$\mathcal{P}_{\text{com}}(R_o) = \sum_{n=1}^{m_L} (-1)^{n+1} \binom{m_L}{n} \exp\left(-\frac{k_L n \phi_c R_o^{\eta_L} K_B T W_b}{P_c G(\theta_m) C_L}\right) \mathcal{L}_{L_c}\left(\frac{k_L n \phi_c R_o^{\eta_L}}{P_c G(\theta_m) C_L}\right) \mathcal{L}_{N_c}\left(\frac{k_L n \phi_c R_o^{\eta_L}}{P_c G(\theta_m) C_L}\right). \quad (49)$$

since $G(\theta_m)$ is a random parameter, let $G(\theta_m) = G_c$ with PDF $f(G_c)$ then:

$$\mathcal{P}_{\text{com}}(R_o) = \sum_{n=1}^{m_L} (-1)^{n+1} \binom{m_L}{n} \int \exp\left(-\frac{k_L n \phi_c R_o^{\eta_L} K_B T W_b}{P_c G_c C_L}\right) \mathcal{L}_{L_c}\left(\frac{k_L n \phi_c R_o^{\eta_L}}{P_c G_c C_L}\right) \mathcal{L}_{N_c}\left(\frac{k_L n \phi_c R_o^{\eta_L}}{P_c G_c C_L}\right) f(G_c) dG_c. \quad (50)$$

Finally, to find the average coverage probability, we take the expectation over R_o whose PDF is given by (7).

REFERENCES

- [1] F. Liu, Y. Cui, C. Masouros, J. Xu, T. X. Han, Y. C. Eldar, and S. Buzzi, "Integrated sensing and communications: Toward dual-functional wireless networks for 6G and beyond," *IEEE journal on selected areas in communications*, vol. 40, no. 6, pp. 1728–1767, 2022.
- [2] J. A. Zhang, M. L. Rahman, K. Wu, X. Huang, Y. J. Guo, S. Chen, and J. Yuan, "Enabling joint communication and radar sensing in mobile networks—A survey," *IEEE Communications Surveys & Tutorials*, vol. 24, no. 1, pp. 306–345, 2021.
- [3] Y. Cui, H. Ding, L. Zhao, and J. An, "Integrated Sensing and Communication: A Network Level Perspective," *IEEE Wireless Communications*, vol. 31, no. 1, pp. 103–109, 2024.
- [4] S. Lu, F. Liu, Y. Li, K. Zhang, H. Huang, J. Zou, X. Li, Y. Dong, F. Dong, J. Zhu, et al., "Integrated sensing and communications: Recent advances and ten open challenges," *IEEE Internet of Things Journal*, 2024.
- [5] Z. Wei, H. Qu, Y. Wang, X. Yuan, H. Wu, Y. Du, K. Han, N. Zhang, and Z. Feng, "Integrated sensing and communication signals toward 5G-A and 6G: A survey," *IEEE Internet of Things Journal*, vol. 10, no. 13, pp. 11068–11092, 2023.
- [6] D. Wen, Y. Zhou, X. Li, Y. Shi, K. Huang, and K. B. Letaief, "A survey on integrated sensing, communication, and computation," *IEEE Communications Surveys & Tutorials*, 2024.
- [7] Y. Nabil, H. ElSawy, S. Al-Dharrab, H. Mostafa, and H. Attia, "Beamwidth Design Tradeoffs in Radar-aided Millimeter-wave Cellular Networks: A Stochastic Geometry Approach," *IEEE Access*, pp. 1–1, 2024.
- [8] R. Li, Z. Xiao, and Y. Zeng, "Towards seamless sensing coverage for cellular multi-Static integrated sensing and communication," *IEEE Transactions on Wireless Communications*, 2023.
- [9] X. Yang, Z. Wei, J. Xu, Y. Fang, H. Wu, and Z. Feng, "Coordinated transmit beamforming for networked ISAC with imperfect CSI and time synchronization," *IEEE Transactions on Wireless Communications*, 2024.
- [10] S. K. Dehkordi, L. Pucci, P. Jung, A. Giorgetti, E. Paolini, and G. Caire, "Multistatic parameter estimation in the near/far field for integrated sensing and communication," *IEEE Trans. Wireless Commun.*, 2024.
- [11] Z. Behdad, Ö. T. Demir, K. W. Sung, E. Björnson, and C. Cavdar, "Multistatic target detection and power allocation for integrated sensing and communication in cell-free massive MIMO," *IEEE Transactions on Wireless Communications*, 2024.
- [12] N. Babu, C. Masouros, C. B. Papadias, and Y. C. Eldar, "Precoding for multi-cell ISAC: from coordinated beamforming to coordinated multipoint and bi-static sensing," *arXiv preprint arXiv:2402.18387*, 2024.
- [13] Z. Wei, R. Xu, Z. Feng, H. Wu, N. Zhang, W. Jiang, and X. Yang, "Symbol-level integrated sensing and communication enabled multiple base stations cooperative sensing," *IEEE Transactions on Vehicular Technology*, 2023.
- [14] N. R. Olson, J. G. Andrews, and R. W. Heath, "Coverage and rate of joint communication and parameter estimation in wireless networks," *IEEE Transactions on Information Theory*, 2023.
- [15] K. Meng, C. Masouros, G. Chen, and F. Liu, "Network-level integrated sensing and communication: Interference management and BS coordination using stochastic geometry," *IEEE Trans. Wireless Commun.*, 2024.
- [16] J. Xu, M. A. Kishk, J. P. Coon, and M.-S. Alouini, "Performance Analysis and Optimal Resource Allocation for Large Scale Joint Sensing and Communication," *IEEE Transactions on Wireless Communications*, 2024.
- [17] Z. Sun, S. Yan, N. Jiang, J. Zhou, and M. Peng, "Performance Analysis of Integrated Sensing and Communication Networks with Blockage Effects," *arXiv preprint arXiv:2403.18621*, 2024.
- [18] A. Salem, K. Meng, C. Masouros, F. Liu, and D. Lopez-Perez, "Rethinking dense cells for integrated sensing and communications: A stochastic geometric view," *IEEE Open Journal of the Communications Society*, 2024.
- [19] K. S. Ali and M. Chafii, "Integrated sensing and communication for large networks using joint detection and a dynamic transmission strategy," *IEEE Transactions on Vehicular Technology*, 2025.
- [20] K. Meng, C. Masouros, A. P. Petropulu, and L. Hanzo, "Cooperative ISAC Networks: Performance Analysis, Scaling Laws and Optimization," *IEEE Transactions on Wireless Communications*, pp. 1–1, 2024.
- [21] Z. Xiao and Y. Zeng, "Waveform design and performance analysis for full-duplex integrated sensing and communication," *IEEE Journal on Selected Areas in Communications*, vol. 40, no. 6, pp. 1823–1837, 2022.
- [22] W. Hong, Z. H. Jiang, C. Yu, J. Zhou, P. Chen, Z. Yu, H. Zhang, B. Yang, X. Pang, M. Jiang, et al., "Multibeam antenna technologies for 5G wireless communications," *IEEE Transactions on Antennas and Propagation*, vol. 65, no. 12, pp. 6231–6249, 2017.
- [23] Z. Wei, L. Zhao, J. Guo, D. W. K. Ng, and J. Yuan, "Multi-Beam NOMA for Hybrid mmWave Systems," *IEEE Transactions on Communications*, vol. 67, no. 2, pp. 1705–1719, 2019.
- [24] X. Yu, J. Zhang, M. Haenggi, and K. B. Letaief, "Coverage analysis for millimeter wave networks: The impact of directional antenna arrays," *IEEE J. Sel. Areas Commun.*, vol. 35, no. 7, pp. 1498–1512, 2017.
- [25] M. R. Akdeniz, Y. Liu, M. K. Samimi, S. Sun, S. Rangan, T. S. Rappaport, and E. Erkip, "Millimeter wave channel modeling and cellular capacity evaluation," *IEEE journal on selected areas in communications*, vol. 32, no. 6, pp. 1164–1179, 2014.
- [26] M. Rebato, J. Park, P. Popovski, E. De Carvalho, and M. Zorzi, "Stochastic geometric coverage analysis in mmWave cellular networks with realistic channel and antenna radiation models," *IEEE Transactions on Communications*, vol. 67, no. 5, pp. 3736–3752, 2019.
- [27] D. K. Barton, *Radar system analysis and modeling*. Artech House, 2004.
- [28] N. J. Willis, *Bistatic radar*, vol. 2. SciTech Publishing, 2005.
- [29] P. Swerling, "Probability of detection for fluctuating targets," *IRE Transactions on Information theory*, vol. 6, no. 2, pp. 269–308, 1960.
- [30] R. E. Kell, "On the derivation of bistatic RCS from monostatic measurements," *Proceedings of the IEEE*, vol. 53, no. 8, pp. 983–988, 1965.
- [31] X. Chen, R. Tharmarasa, M. Pelletier, and T. Kirubarajan, "Integrated clutter estimation and target tracking using Poisson point processes," *IEEE Trans. Aerosp. Electron. Syst.*, vol. 48, no. 2, pp. 1210–1235, 2012.
- [32] D. A. Shnidman, "Radar detection in clutter," *IEEE Transactions on Aerospace and Electronic Systems*, vol. 41, no. 3, pp. 1056–1067, 2005.
- [33] M. L. Rahman, J. A. Zhang, X. Huang, Y. J. Guo, and R. W. Heath, "Framework for a perceptive mobile network using joint communication and radar sensing," *IEEE Transactions on Aerospace and Electronic Systems*, vol. 56, no. 3, pp. 1926–1941, 2019.
- [34] M. Sekine and Y. Mao, *Weibull radar clutter*. No. 3, IET, 1990.
- [35] F. Liu, Y. Xiong, K. Wan, T. X. Han, and G. Caire, "Deterministic-random tradeoff of integrated sensing and communications in Gaussian channels: A rate-distortion perspective," in *2023 IEEE International Symposium on Information Theory (ISIT)*, pp. 2326–2331, IEEE, 2023.
- [36] B. Tang and J. Li, "Spectrally constrained MIMO radar waveform design based on mutual information," *IEEE Transactions on Signal Processing*, vol. 67, no. 3, pp. 821–834, 2018.
- [37] H. ElSawy, W. Dai, M.-S. Alouini, and M. Z. Win, "Base Station Ordering for Emergency Call Localization in Ultra-Dense Cellular Networks," *IEEE Access*, vol. 6, pp. 301–315, 2018.
- [38] H. ElSawy, A. Sultan-Salem, M.-S. Alouini, and M. Z. Win, "Modeling and analysis of cellular networks using stochastic geometry: A tutorial," *IEEE Communications Surveys & Tutorials*, vol. 19, no. 1, pp. 167–203, 2016.
- [39] S. S. Ram and G. Ghatak, "Estimation of bistatic radar detection performance under discrete clutter conditions using stochastic geometry," in *2022 IEEE Radar Conference (RadarConf22)*, pp. 1–6, IEEE, 2022.
- [40] Y. Yang and R. S. Blum, "Phase synchronization for coherent MIMO radar: Algorithms and their analysis," *IEEE Transactions on Signal Processing*, vol. 59, no. 11, pp. 5538–5557, 2011.
- [41] M. Sadeghi, F. Behnia, R. Amiri, and A. Farina, "Target localization geometry gain in distributed MIMO radar," *IEEE Transactions on Signal Processing*, vol. 69, pp. 1642–1652, 2021.
- [42] N. Bahadori, N. Namvar, B. Kelley, and A. Homaifar, "Device-to-device communications in millimeter wave band: Impact of beam alignment error," in *2019 Wireless Telecommunications Symposium (WTS)*, IEEE, 2019.
- [43] K. S. Ali, H. ElSawy, and M.-S. Alouini, "Modeling cellular networks with full-duplex D2D communication: A stochastic geometry approach," *IEEE Transactions on Communications*, vol. 64, no. 10, pp. 4409–4424, 2016.
- [44] H. Alzer, "On some inequalities for the incomplete gamma function," *Mathematics of Computation*, vol. 66, no. 218, pp. 771–778, 1997.